Self-regulated plasma heat flux mitigation due to liquid Sn vapor shielding

G.G. van Eden*, T.W. Morgan, D.U.B. Aussems, M.A. van den Berg, K. Bystrov, and M.C.M. van de Sanden
FOM institute DIFFER, Dutch Institute for Fundamental Energy Research,
*Association EURATOM-FOM, 5612 AJ, Eindhoven, The Netherlands**
(Dated: January 23, 2016)

A steady-state high-flux H or He plasma beam was balanced against the pressure of a Sn vapor cloud for the first time, resulting in a self-regulated heat flux intensity near the liquid surface. A temperature response of the liquid surface characterized by a decoupling from the received heating power and significant cooling of the plasma in the neutral Sn cloud were observed. The plasma heat flux impinging on the target was found to be mitigated as heat was partially dissipated by volumetric processes in the vapor cloud rather than wholly by surface effects. These results motivate further exploration of liquid metal solutions to the critical challenge of heat- and particle flux handling in fusion power plants.

Designing an efficacious interface between an intense plasma flux and a solid material has been a challenge for many decades and is among the top issues in realizing fusion energy as a viable energy source on Earth. Plasma-solid interactions under fusion divertor conditions cause continuous material erosion and may result in performance degradation of the plasma facing components [1–3]. An alternative path is opened by exploiting liquid metals as an interface between the plasma and solid material world [4], which can potentially alleviate many of the problems of heat exhaust in the divertor. Understanding the unique power loss channels of liquid metals in contact with a plasma is also highly relevant for other applications such as metal-arc welding [5].

Additional power handling capabilities such as evaporative cooling [6, 7] and the vapor shielding effect [8, 9] are inherently available for a liquid surface. The meaning of vapor shielding encompasses several physical processes. Firstly, the presence of a neutral cloud in front of the target is foreseen to absorb power by excitation and ionization of its species. Subsequent radiation occurs isotropically which reduces the areal power density. Secondly, the cloud of neutrals leads directly to mass transport losses but also to friction and recombination of impinging plasma particles, ultimately reducing the energy flux to the surface.

In this letter, for the first time, we provide experimental evidence of steady-state vapor shielding at fusion divertor relevant plasma heat- (0.5-22 $\mathrm{MW\,m^{-2}}$) and particle fluxes ($>10^{24}\,\mathrm{m^{-2}\,s^{-1}}$). In addition, the experimental validation of using Sn for high heat flux applications as previously predicted by modeling [10] is now provided. The work was motivated by the question of what the potential of vapor shielding is in protecting a surface. To ensure a vapor pressure of similar magnitude as the plasma pressure, the Sn targets were intentionally badly cooled. The power handling characteristics of liquid Sn were compared to those of solid Mo (high heat handling capability and substrate material for Sn) while exposed to similar plasma conditions and target cooling in the linear plasma generator Pilot-PSI [11].

The thermal response of the liquid upon receiving an intense plasma heat flux up to $22\,\mathrm{MW\,m^{-2}}$ lasting 5-20 s is described. A self-regulated plasma heat flux mitigation by the liquid/vapor system and cooling of the electrons in the vapor cloud is observed, leading to an approximately 30% reduction in heat flux measured by calorimetry, compared to a solid Mo target. Up to 20% of this missing power could be associated with evaporative cooling whereas >80% is dissipated via other processes, including radiation from the plasma and cooling and recombination of the plasma due to the vapor cloud.

The linear plasma device Pilot-PSI [11] employs a wall-stabilized thermal arc source [12] to produce a high-flux plasma which is subsequently confined into a beam by an axial B-field (0.4-1.2 T). A power scan of the source resulted in H or He particle- (Γ_{part}) and heat fluxes (q) of 0.9-6.4×$10^{24}\,\mathrm{m^{-2}\,s^{-1}}$ and 0.5-22 $\mathrm{MW\,m^{-2}}$ respectively impinging on the target center. The particle- and heat fluxes as function of the plasma beam radius can be well represented by a 2D Gaussian function (FWHM≈10.4 mm). The values were calculated based on the plasma parameters 11 mm in front of the solid Mo target obtained from Thomson Scattering (TS) measurements [13]. Heat fluxes were calculated as in [14] assuming $T_i \approx T_e$ (the source produces a thermal plasma), that flow was adiabatic with an isotropic pressure and that the sheath heat transmission coefficient was set equal to 7.

As TS was not available, the upstream plasma conditions during Sn exposures have been assessed from reference shots on Mo, where we assume that the upstream plasma power should be highly similar for both targets. This is justified as the I-V characteristics of the plasma source were similar for discharges on Mo and Sn targets and no traces of Sn were found in the vicinity of the source after operation. Also, the mean free path of the Sn neutrals (6 mm) is much shorter than the distance to the plasma source (560 mm). The incoming heat flux which must be balanced by heat removal processes in equilibrium conditions is therefore the reference heat flux (q_{ref})

* g.g.vaneden@differ.nl

which is the measured heat flux received by a Mo target for identical Pilot-PSI operational settings.

A 2-channel spectrometer (Avantes ULS2048) was used to measure the radiation intensity in the 299-579 nm range. The detector was focused at the target center (∼15° normal to surface) with a spot size of 1 mm. The surface temperature was measured using both an IR camera (FLIR SC7500MB, 4.5 kHz) and a multi-wavelength spectropyrometer (FAR associates FMPI). A temperature-dependent emissivity was applied, previously obtained by comparing the IR and pyrometer data. We assume that any IR emission from the vapor cloud itself is negligible as its density is 8 orders of magnitude lower than that of the liquid. Finally, Sn neutral emission was recorded by a fast visible camera (Phantom V12, 10 kHz) equipped with a 452.5 nm SnI filter positioned tangentially to the target. The targets consist of a 3 mm deep Mo cup where the Sn content is held secured by a stack of W meshes, see Fig. 1. This design is based on the capillary-porous-system (CPS) principle [15].

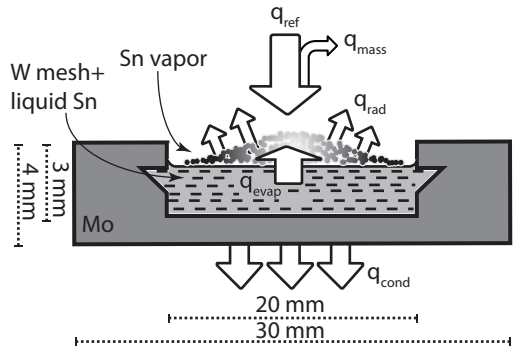

FIG. 1. Cross-section drawing of the Mo CPS target filled with Sn. Sn is held in place by a W mesh structure. The Sn surface receives a plasma heat flux (q_{ref}) which leads to evaporation and subsequent vapor formation in front of the target. The power is dissipated via evaporation and direct mass transport (q_{evap}), radiation by the Sn vapor cloud (q_{rad}) and mass transport resulting from CX and recombination processes (q_{mass}). The remaining heat is conducted to the cooling water (q_{cond}).

The plasma heat flux (q_{ref}) is dissipated via a number of processes. Firstly, power is dissipated by vaporization if evaporated neutrals do not return to the surface (q_{evap}). Secondly, power is lost by radiation of Sn neutrals and ions in the vapor cloud (q_{rad}) and mass transport (q_{mass}) from the plasma as a result of Charge Exchange (CX) and recombination processes. The remaining heat is transferred to the Mo cup (and subsequently cooling water) via conduction and convection of the liquid Sn (q_{cond}). Only low ionization stages of Sn are reached due to the low temperature in the plasma beam. Ionization to much higher states is expected in a tokamak, which may affect Sn transport and the heat handling scheme for that geometry.

Figure 2 shows the temperature evolution at the center of the liquid Sn and solid Mo surfaces while exposed to $q_{ref} = 16\,\mathrm{MW\,m^{-2}}$. Notable differences in thermal response are observed. Firstly, an approximately steady-state surface temperature is reached after ∼0.5 s on the liquid surface while the Mo temperature still rises. Secondly, the temperature ramp in the Sn case does not follow a conduction-based cooling curve, where the temperature increases following Newton's law of cooling until the conducted heat equals the received plasma heating as for the Mo case. Results from 3D finite element modeling using ANSYS [16] for the same q_{ref} and target materials are shown as well. The mesh has been accounted for in the model for Sn by assuming a 6.25 weight percent of W and applying thermal properties of the mixed material. Only conduction-based cooling has been taken into account and the absorbed heat by the cooling structure has been modeled to match the experimental results for Mo. Comparing the model with the experimental data for Sn, a reduction of ∼700 K compared to expectations at the end of the discharge is observed which indicates the presence of additional heat dissipation channels for the liquid. It should be noted that the conduction based model predicts a higher surface temperature for Sn than Mo due to the lower thermal conductivity of the former. The experiment shows however a lower final surface temperature for Sn compared to Mo which gives a clear demonstration that other power loss processes are important.

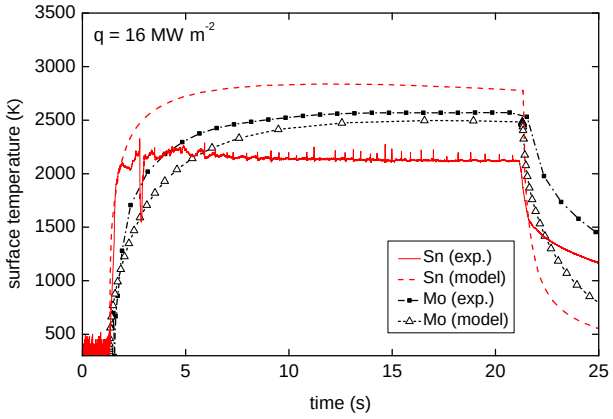

FIG. 2. (color online). A comparison of the central surface temperature evolution of liquid Sn and solid Mo during experiment and ANSYS simulations for q_{ref}=16 MWm^{-2}. The steady-state temperature of Sn reduces significantly due to vapor shielding compared to the conduction-based model without vapor shielding.

Figure 3 shows the central surface temperature at the end of 20 s plasma discharges for both sample types as a function of q_{ref}. It is striking to see that the surface temperature of the liquid Sn is almost independent of the applied heat flux. The final temperature at the solid Mo target increases with rising plasma power as expected. The data point for Mo at 22 MW m^{-2} represents the temperature after a 5 s discharge (to avoid melting the target) and did not reach an equilibrium tempera-

ture.

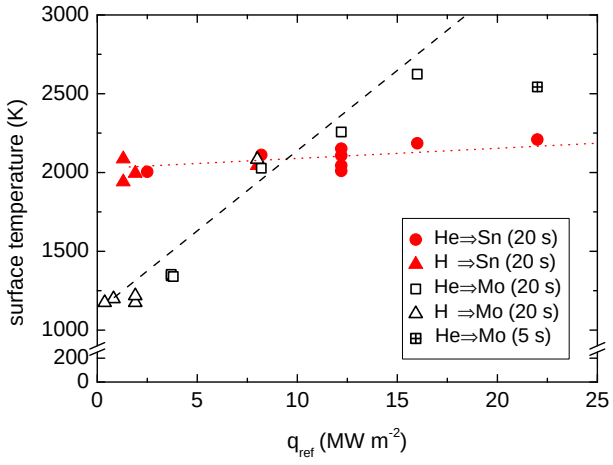

FIG. 3. (color online). Temperature of the target surface center after 20 s of plasma exposure for liquid Sn and solid Mo. The lines are drawn to guide the eye. The surface temperature of liquid Sn is almost independent of q_{ref} for the given parameter space. The data point for Mo at 22 MWm^{-2} had a 5 s shot duration to prevent melting the target.

The magnitude of Γ_{part} versus the evaporation flux is assessed now. The vapor pressure (p_v) as function of surface temperature (T (K)) is calculated as in [17]: $\lg(p_v) = 10.268 - 15332/T$. The flux of particles leaving the surface by evaporation (Γ_{evap}) at a temperature T (K) is assumed to follow from the Langmuir evaporation law [18], $\Gamma_{evap}(T) = p_v/\sqrt{2\pi m k_B T}$, where k_B represents the Boltzmann constant and m the mass of Sn (kg). Fig. 4 shows Γ_{evap} (calculated using the temperatures as shown in Fig. 3) versus Γ_{part} in the beam center. It is clear from this figure that Γ_{evap} increases linearly in

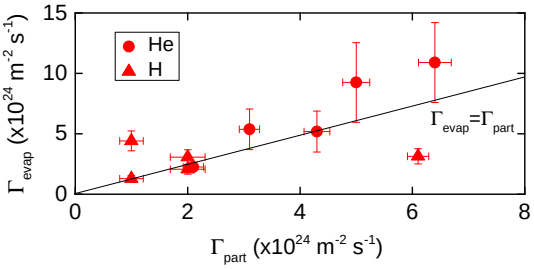

FIG. 4. (color online). Evaporation flux (Γ_{evap}) versus the plasma particle flux (Γ_{part}) in the center of the beam for He and H discharges. The solid line represents a perfect equilibrium between plasma- and evaporation flux.

proportion to Γ_{part} for all He discharges and roughly follows Γ_{evap}=1.6×Γ_{part}. The Sn evaporation flux during H discharges is seen to remain approximately at the same level. It is proposed that because of the lower mass of H compared to He, the former is affected more strongly by momentum loss via collisions with Sn, therefore resulting in a lower surface temperature and thus evaporation rate.

The temperature rise of the cooling water was used to determine the average deposited power during each discharge. The average conducted power per unit area, q_{cond}, is $\langle P_{cond}\rangle/\pi a^2$ where a is the target radius. Results of $\langle P_{cond}\rangle$ are shown in Fig. 5a. The non-linearity of $\langle P_{cond}\rangle$ at small q_{ref} (and offset) is attributed to a systematic error in the value of the cooling water speed. Further analysis is not affected as ΔP_{cond} is calculated. The total transferred heat is lower for all exposures on Sn compared to exposures on Mo for q_{ref}>2.5 MW m^{-2} and indistinguishable within or below this. The difference in conducted power between the Mo and Sn target increases with increasing q_{ref}. The question is therefore by what other dissipation mechanisms this power is removed.

Figure 5b shows the difference in conducted power between Sn and Mo at equal q_{ref}: $\langle \Delta P_{cond}\rangle = \langle P_{cond,Mo}\rangle - \langle P_{cond,Sn}\rangle$. As a result of the Gaussian profile of

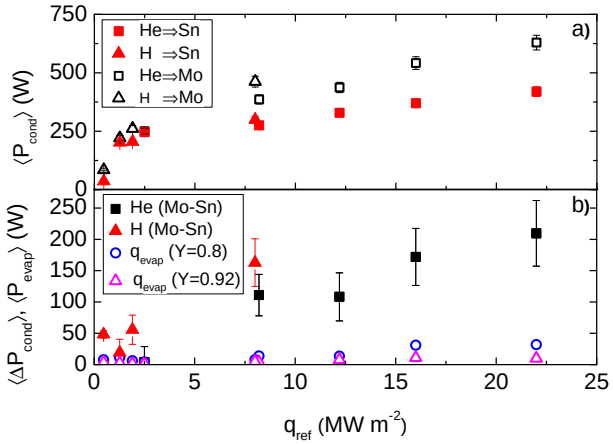

FIG. 5. (color online). Power transferred to cooling water as function of q_{ref} for both target types (a) and the difference in conducted power between Mo and Sn (b). The open circles in b indicate the power dissipated via evaporation assuming Y=0.8. The inverted triangles represent the lost evaporative power in case of Y=0.92 [19].

the plasma parameters in the beam, the surface temperature is a circularly symmetric profile and can be well represented by a Gaussian function: $T(r) = T_{max}\exp(-r^2/2\sigma^2)$. The total power dissipated due to evaporation can now be calculated by multiplying this by the latent heat of vaporization and integrating over the target area:

$$\langle P_{evap}\rangle = (1-Y)\frac{\Delta H_{evap}}{N_A}\int_0^{2\pi}\int_0^{a}\Gamma_{evap}(T(r))r\,dr\,d\theta, \quad (1)$$

where N_A represents the Avogadro constant and Y the particle redeposition fraction.

The peak surface temperature (T_{max}) during the Sn exposures is presented in Fig. 3. By measuring the FWHM of each Gaussian temperature profile, $T(r)$ is obtained and $\langle P_{evap}\rangle$ is calculated using equation 1. Consequently, $q_{evap} = \langle P_{evap}\rangle/\pi a^2$.

As the ionization energy of Sn is only 7.34 eV, a large fraction of Sn atoms are ionized and consequently entrained in the plasma and redeposited onto the surface. The removed power for these particles is redeposited onto the surface and is thus not a power loss channel. Redeposition rates of Sn in Pilot-PSI at similar conditions have been previously reported and revealed fractions $Y \geq 0.92$ [19]. Also, a depletion of Sn in the top layer of mesh in the target was observed after 100 s of plasma exposure, resulting in a loss of 0.45 g Sn. When assuming evaporation without redeposition, 3.4 g is lost for the same duration, yielding a redeposition rate of 87%. The lost power by evaporation for Y=0.92 and Y=0.8 (i.e. 8 and 20% lost particles) are shown in Fig. 5b. The latter represents a lower bound, accounting for uncertainties in assessing the depletion of Sn in the sample.

The effect of the vapor cloud on the electron temperature (T_e) was studied using spectroscopic analysis. Fig. 6 shows a spectrum obtained during a H discharge [20]. The requirement of Partial Local Thermal Equilibrium (PLTE) for our H plasma (typically $n_e = 10^{20}\,\mathrm{m}^{-3}$ and $T_e = 1\,\mathrm{eV}$) is fulfilled for energy levels n>4 [21]. The density of the upper state (n_j) is proportional to its line intensity (I_j): $n_j \propto (4\pi/A_{ji})I_j$ where A_{ji} represents the Einstein coefficient for this particular transition.

The emission intensities of the following H lines were used: 9-2 (383 nm), 8-2 (388.9 nm), 7-2 (397 nm), 6-2 (410.2 nm) and 5-2 (434 nm) (Balmer series with n>4) followed by a background subtraction. For He discharges, unobscured lines for analysis where selected for each discharge separately from the following set: 1s9s-1s2p (360 nm), 1s8d-1s2p (363.5 nm), 1s8s-1s2p (365.3 nm), 1s7d-1s2p (370.6 nm), 1s6d-1s2p (382.1 nm), 1s6s-1s2p (386.9 nm), 1s4d-1s2p (447.3 nm).

The ratio of densities of such lines gives T_e, as expressed by the Boltzmann relation [21]:

$$\frac{n_j}{n_i} = \frac{g_j}{g_i} e^{-(E_j - E_i)/k_B T_e}. \qquad (2)$$

The inset in Fig. 6 shows n_j/g_j versus the upper state energy level (E_j) for a series of high-n H transitions. The PLTE requirement is regarded to be fulfilled when this fit yields a straight line [22]. The inverse slope of the fit then yields T_e [23]. For a given plasma discharge, T_e was determined from averaging multiple spectra during the phase of constant B-field in the discharge.

The applicability of this method was verified by cross-checking T_e with values obtained from TS during H exposures on Mo. The methods were seen to yield similar values for T_e as shown in Fig. 7a which gives confidence in the procedure. T_e in the Sn/H and Sn/He near-surface plasma are shown in Fig. 7b. It is striking to see that T_e in front of the liquid surface is roughly 80% lower than in case of the solid target and that it is approximately constant at ~0.5 eV for q_{ref}>5 MW m^{-2}. As the region of highest radiation levels lies just above the surface, the emission we observe comes predominantly from

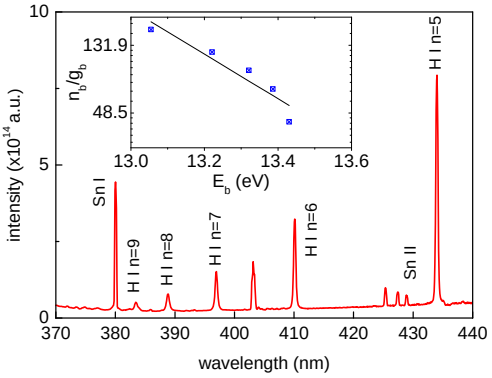

FIG. 6. (color online). Typical spectrum showing high-n states of H. The inset gives an example of the Boltzmann method: n_j/g_j is plotted versus the upper state energy level E_b. The inverse slope of the fitted line gives T_e.

there. Therefore, T_e obtained by the Boltzmann method gives the conditions in the Sn/He and Sn/H near-surface plasma.

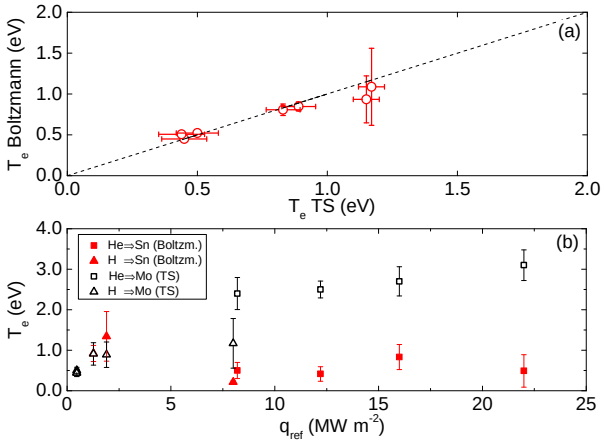

FIG. 7. (color online). T_e as function of q_{ref} for the Boltzmann and TS method compared for exposures on Mo (a). Comparison of T_e near a liquid Sn and solid Mo surface for H and He exposures (b). T_e is found to be significantly lower in front of the liquid surface compared to the solid reference (especially in the case of He).

The reduction in T_e by interaction with the vapor cloud is interpreted to be a two-step process. Firstly, as the ion-neutral cross-section is much larger than the electron-neutral cross-section due to the mass difference between electrons and ions, predominantly it is the ions that lose their energy by elastic collisions with Sn neutrals. Secondly, the electrons are cooled by energy exchange with ions which increases as T_e decreases [24]. The ionization and recombination rates for He at 2 eV and n_e=10^{20} m^{-3} are almost equal whereas the recombination rate dominates the ionization rate by a factor >10^6 for T_e<1 eV at this density [25]. Given the measured T_e as shown in Fig. 7, the plasma transitions from an ionizing to a recombining regime upon entering the vapor cloud.

It may be noted that Fig. 7 shows that the decrease in T_e at a given q_{ref} is larger for H than for He. This observation could be explained by the additional presence of Molecular Assisted Recombination (MAR) processes leading to increased H recombination by a factor of 8-10 at low values of T_e [26]. For both plasma species we may also consider that CX processes with the neutral Sn play a direct role to neutralize the hot ions which are then no longer confined by the B-field. Overall these processes are proposed to account for a significant power loss since neutralized particles leave the plasma beam carrying energy away (q_{mass}). This loss channel is in addition to evaporated Sn particles that do not return to the surface (q_{evap}).

In summary, balancing the steady-state plasma pressure with the vapor pressure in front of a liquid surface led to a range of interlinked phenomena resulting in a reduced target heat flux. Power is dissipated via evaporation (up to 20%), radiation and mass loss, which reduces the surface heat load by $\sim$1/3 compared to the solid case. T_e in front of the Sn target is measured to decrease by $\sim$80 % compared to the solid reference, indicating that mass transport processes are playing an important or even dominant role. The overall effect appears self-regulatory, where an increase of heat- and particle flux is balanced by an increased evaporation flux leading to an approximately constant heat load received by the liquid PFC. While the issue of Sn exceeding the tolerable impurity fraction in a magnetic fusion plasma could not be addressed due to differences in magnetic geometry and vapor cloud production, this work takes a critical step towards the design of a liquid metal solution for a fusion power plant, namely, the demonstration of the effectiveness of vapor shielding.

The authors wish to thank the Pilot-PSI technical staff and Ronald Wolbeer for the manufacturing of the Sn targets and Egbert Westerhof and Gieljan de Vries for providing valuable input to the manuscript. This work is part of the research program of the Stichting voor Fundamenteel Onderzoek der Materie (FOM), which is financially supported by the Nederlandse Organisatie voor Wetenschappelijk Onderzoek (NWO). It is supported by the European Communities under the contract of Association between EURATOM and FOM and was conducted within the framework of the European Fusion Programme.

[1] A.W. Leonard, A. Herrmann, K. Itami *et. al.*, *J. Nucl. Mat.*, **266-269**, 109-117 (1999).
[2] R.A. Pitts, S. Carpentier, F. Escourbiac *et. al.*, *J. Nucl. Mat.*, **438**, S48-S56 (2013).
[3] G.G. van Eden, T.W. Morgan, H.J. van der Meiden *et. al.*, *Nucl. Fusion*, **54**, 123010 (2014).
[4] M.A. Abdou, The APEX Team, N. Morley *et. al.*, *Fusion Eng. Des.*, **54**, 181-247 (2001).
[5] A. Murphy, *J. Phys. D.*, **43**, 434001 (2010).
[6] Y. Nagayama, *Fusion Eng. Des.*, **84**, 1380-1383, (2009).
[7] V.A. Evtikhin, A.V. Vertkov, I.E. Lyublinski, *J. Nucl. Mat.*, **307-311**, 1664-1669 (2002).
[8] T. Sizyuk and A. Hassanein, *Nucl. Fusion*, **54**, 023004 (2014).
[9] J. Gilligan, D. Hahn, R. Mohanti, *J. Nucl. Mat.*, **162-164**, 957-963 (1989).
[10] J.W. Coenen, G. De Temmerman, G. Federici *et. al.*, *Physica Scripta*, **T159**, 014037 (2014).
[11] G.J. van Rooij, V.P. Veremiyenko, W.J. Goedheer *et. al. al.*, *Appl. Phys. Lett.*, **90**, 121501 (2007).
[12] W.A.J. Vijvers, C.A.J. van Gils, W.J. Goedheer *et. al.*, *Physics of plasmas*, **15**, 093507 (2008).
[13] H.J. van der Meiden, R.S. Al, C.J. Barth *et. al.*, *Rev. Sci. Instrum.*, **79**, 013505 (2008).
[14] P.C. Stangeby, *The Plasma Boundary of Magnetic Fusion Devices*, Taylor & Francis (2000).
[15] V.A. Evtikhin, I.E. Lyublinksi, A.V. Vertkov *et. al.*, *J. Nucl. Mat.*, **271-272**, 396-400 (1999).
[16] *ANSYS Multiphysics 15.0, user manual*
[17] C.B. Alcock, V.P. Itkin, M.K. Horrigan, *Canadian Metallurgical Quarterly*, **23**, 309 (1984).
[18] I. Langmuir, *Proc. Nat. Acad. Sci. U.S.A.*, **45**, 452-452 (1917).
[19] T.W. Morgan, D.C.M. van den Bekerom, G. De Temmerman, *J. Nucl. Mat.*, **463**, 1256-1259 (2015).
[20] NIST, `http://www.nist.gov/pml/data/asd.cfm`.
[21] H. Griem, *Principles of Plasma Spectroscopy*, Cambridge University Press (1997).
[22] D. Nishijima, U. Wenzel, K. Ohsumi *et. al.*, *Plasma Phys. Controlled Fusion*, **44**, 597-610 (2002).
[23] D.U.B. Aussems, D. Nishijima, C. Brandt, *J. Appl. Phys.*, **116**, 063301 (2014).
[24] N. Ohno, D. Nishijima, S. Takamura *et. al.*, *Nucl. Fusion*, **41**, 1055 (2001).
[25] H.P. Summers, *Atomic Data and Analysis Structure User Manual* (2004).
[26] A.Y. Pigarov, *Physica Scripta*, **T96**, 16-31 (2002).